RESEARCH ARTICLE

NANO · MICRO small
www.small-journal.com

PVDF-HFP Based, Quasi-Solid Nanocomposite Electrolytes for Lithium Metal Batteries

*Eleonora Carena, Lorenzo Mezzomo, Nicholas Vallana, Nicole Ceribelli, Giovanni Di Liberto, Silvia Mostoni, Chiara Ferrara, Michele Mauri, Roberto Lorenzi, Livia Giordano, Riccardo Ruffo, and Piercarlo Mustarelli**

Composite polymer electrolytes are systems of choice for future solid-state lithium metal batteries (LMBs). Poly(vinylidene fluoride-co-hexafluoropropylene) (PVDF-HFP) is among the most interesting matrices to develop new generation quasi-solid electrolytes (QSEs). Here it is reported on nanocomposites made of PVDF-HFP and pegylated SiO_2 nanoparticles. Silica-based hybrid nanofillers are obtained by grafting chains of poly(ethylene glycol) methyl ether (PEG) with different molecular weight on the surface of silica nanoparticles. The functionalized nanofiller improves the mechanical, transport and electrochemical properties of the QSEs, which show good ionic conductivity values and high resistance against dendrite penetration, ensuring boosted long and safe device operation. The most promising result is obtained by dispersing 5 wt% of SiO_2 functionalized with short PEG chains (PEG_{750}, Mw = 750 g mol^{-1}) in the PVDF-HFP matrix with an ease solvent-casting procedure. It shows ionic conductivity of 0.1 mS cm^{-1} at 25 °C, more than 250 h resistance to stripping/plating, and impressive results during cycling tests in LMB with $LiFePO_4$ cathode.

1. Introduction

Lithium-ion batteries (LIBs) are accompanying the progressive development of society, with relevant applications in everyday life, including consumer electronics, grid levelling, and automotive. Despite the favorable characteristics that enabled their establishment in the market, such as high energy density, superior cycling stability, and lightweight, the rapidly growing automotive sector calls for still higher specific energy and power, increased safety, and lower cost.[1,2] Metallic lithium is an ideal anode material for rechargeable batteries, thanks to its high theoretical specific capacity (3860 mAh g^{-1}), low density (0.534 g cm^{-3}), and low electrochemical potential (−3.040 V vs. SHE).[3,4] However, lithium metal batteries (LMBs) are still far from full industrial deployment because of some relevant issues. The two major challenges are represented by interface instability and uncontrolled lithium dendritic growth. These metallic microstructures are responsible for the decrease of the coulombic efficiency of the cell and the shortening of operating life, because they generate internal short circuits, triggering fires or explosions.[5,6] To solve this problem, liquid electrolytes could be replaced with solid-state (SSEs) or quasi-solid (QSEs) electrolytes, which exhibit good ionic conductivity and appropriate electrochemical stability, being at the same time sufficiently resistant to act as physical barriers.[2] They can help in improving the interface stability, and inhibiting the dendritic growth; finally, by replacing the traditional organic-based liquid electrolytes, they can also improve the overall safety, decreasing the risk of thermal runaway and explosion.[6–11]

Nowadays, poly(ethylene oxide) (PEO)-based electrolytes are the most explored SSEs. However, their room temperature ionic conductivity is not satisfactory, and polymer crystallization further reduces their performance.[12–14] In addition, they suffer of inadequate mechanical strength.[15] Therefore, other SSEs are currently being studied following different approaches, e.g.: i) the choice of a mechanically stronger polymer matrix that can contrast dendritic growth, or ii) the introduction of inorganic ceramic filler nanoparticles (NPs) that may improve the mechanical properties and create additional conducting pathways for ions.[13,16] Poly(vinylidene fluoride) (PVDF) shows excellent thermal and chemical stability, high mechanical strength, high dielectric constant and wide electrochemical stability window.[17,18] To improve the membrane's processability, poly(vinylidene fluoride-co-hexafluoropropylene) (PVDF-HFP) copolymers can be used thanks to their lower crystallinity.[19] To overcome the drawback of reduced mechanical stability in the less crystalline matrix, it

E. Carena, L. Mezzomo, N. Vallana, N. Ceribelli, G. Di Liberto, S. Mostoni, C. Ferrara, M. Mauri, R. Lorenzi, L. Giordano, R. Ruffo, P. Mustarelli
Department of Materials Science of University of Milano Bicocca
Via Cozzi 55, Milano 20125, Italy
E-mail: piercarlo.mustarelli@unimib.it

E. Carena, L. Mezzomo, N. Vallana, C. Ferrara, L. Giordano, R. Ruffo, P. Mustarelli
GISEL-INSTM
Unit of Milano Bicocca
Via Cozzi 55, Milano 20125, Italy

The ORCID identification number(s) for the author(s) of this article can be found under https://doi.org/10.1002/smll.202311805

DOI: 10.1002/smll.202311805

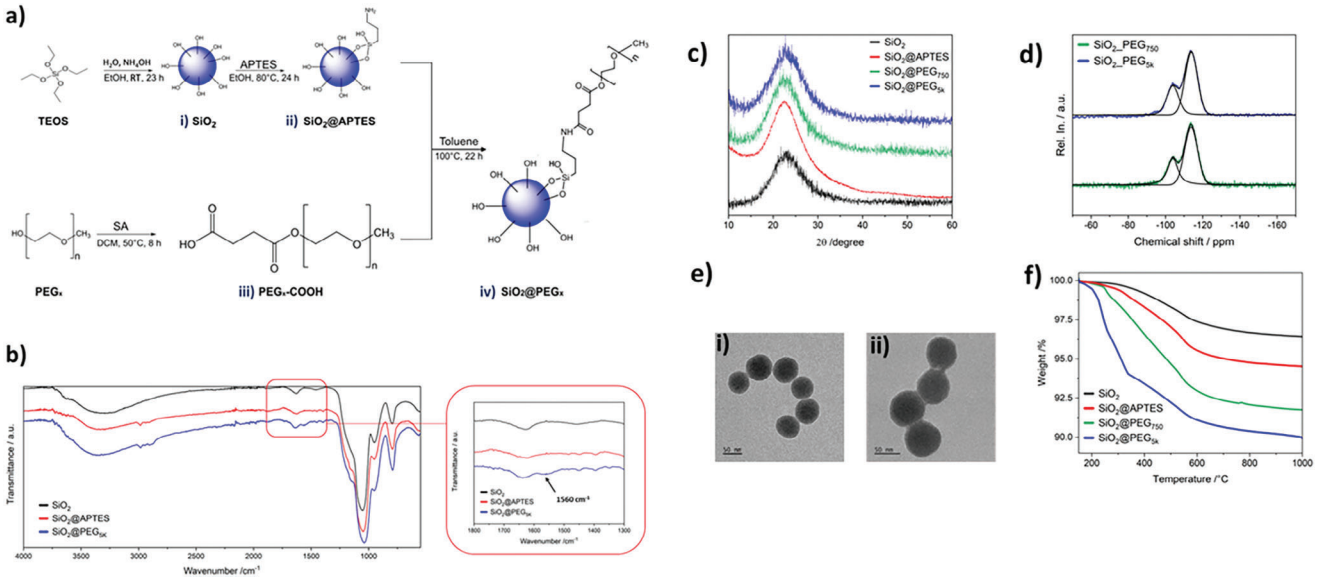

Figure 1. a) Scheme of hybrid filler preparation through a four-steps synthesis: i) synthesis of SiO_2 NPs; ii) SiO_2 NPs functionalization with APTES; iii) activation of PEG chains with terminal -COOH groups (PEG_x-COOH); iv) SiO_2 grafting with PEG_x-COOH (SiO_2@PEG_x); b) FT-IR spectra of SiO_2, SiO_2@APTES and SiO_2@PEG_{5K} to qualitatively verify the progress of the reactions; c) XRD pattern of SiO_2, SiO_2@APTES and SiO_2@PEG_x to check the amorphous nature of the NPs, which results unchanged through the synthetic steps; d) ^{29}Si MAS-NMR spectra of SiO_2@PEG_{5K} and SiO_2@PEG_{750}; e) TEM analysis of pristine SiO_2 (i) and SiO_2@PEG_{5K} (ii) to evidence qualitatively the presence of PEG_x-functionalization; f) Thermal degradation profiles of SiO_2, SiO_2@APTES and SiO_2@PEG_x.

is possible to reinforce the membrane with the addition of inorganic fillers, exploiting the full potential expressed by composite solid-state electrolytes (CSSEs).[20]

Recent studies[21,22] showed that it is possible to synthesize PVDF-based self-standing membranes, characterized by high ionic conductivity, without explicitly adding solvents or plasticizers. Indeed, the transport of lithium ions is ensured by the residual solvent content exploited for the membrane preparation (e.g., dimethylformamide, DMF), which is not free in the matrix, but rather present as a $[Li(DMF)_x]^+$ complex ($x \leq 3.29$), and is transported across polymer chains.[23,24] Recently, in a companion paper we have fully addressed the transport mechanism of such a system.[25] However, independent on the physical chemistry of the ion transport, these systems work well, and could provide promising performance and greater safety in LMBs.

Here we reported on the fabrication of PVDF-HFP-based nanocomposite electrolyte membranes encompassing SiO_2 NPs functionalized on the surface with poly(ethylene glycol) of different molecular weight (PEG_x, x = 750, 5000 g mol^{-1}). Li^+ transport was improved by filler addition, chiefly when the surface functionalization is obtained with short PEG_{750} chains. At the same time, the NPs mechanically reinforced the QSE to inhibit dendritic growth. The nanocomposite membranes showed ionic conductivity, $\sigma > 0.1$ mS cm^{-1} at the room temperature (25 °C). They were tested in symmetric cells with lithium electrodes subjected to increasing current density, and the nanocomposite electrolytes could withstand metal deposition during stripping and plating analysis, differently from the membrane without any dispersed filler, which otherwise led to premature cell failure. Finally, the most promising sample was tested in complete LMB, using $LiFePO_4$ (LFP) as the cathode material.

2. Results and Discussion

2.1. Hybrid Silica Filler Synthesis

The products prepared following the procedure reported in **Figure 1a** were characterized to ascertain their effective properties and composition at each synthetic step.

The FTIR spectrum of SiO_2 NPs (Figure 1b) revealed the presence of an intense peak at 1053 cm^{-1}, related to Si-O-Si stretching and of a peak at 949 cm^{-1}, due to Si-O-H stretching.[26,27] The latter peak decreased in intensity in the spectrum of SiO_2@APTES upon functionalization with APTES, due to the consumption of the surface OH groups of SiO_2 NPs. Besides, the appearance of two peaks at 2983 and 2834 cm^{-1}, attributed to the stretching of the C—H bond of the APTES propyl chain, confirmed the proper surface grafting.[28–31] After functionalization with PEG_x, an increase in the intensity of these peaks was connected to the presence of alkyl chains on the silica surface. The interaction between PEG_x-COOH and the amine groups of APTES is suggested by the formation of a low-intensity peak at 1560 cm^{-1} in the spectrum of SiO_2@PEG_X (absent in the spectrum of SiO_2 and SiO_2@APTES), possibly attributable to the N-H bending of the amide group formed during the reaction with PEG_X.[32] Furthermore, the absence of the peak at 1734 cm^{-1} in the spectrum of SiO_2@PEG_X, associated with the stretching of the C═O bond of the carboxyl groups of PEG_x-COOH (Figure S1, Supporting Information), suggested the absence of free -COOH groups in the final product.

The behavior of the multistep reaction of Figure 1a was also checked by evaluating the ζ-potential during all the synthetic steps, that gives an indication of the surface charge of the water-dispersed powders. Pristine silica samples (Figure 1a-i)

Table 1. Weight loss ($\Delta W_{150\text{-}1000}$ (%)), degree of functionalization achieved expressed in relation to the mass of pristine silica (wt%/weight$_{Silica}$), reaction yield and ratio between the numbers of APTES chains and PEG$_x$ chains grafted on the NPs for products obtained in steps 2 and 4. The last column summarizes the functionalization obtained considering the two final products (SiO_2@PEG$_{750}$ and SiO_2@PEG$_{5k}$).

	$\Delta W_{150\text{-}1000}$ (%)	Functionalization (wt%/weight$_{Silica}$)	Reaction yield (%)	APTES/PEG$_x$ (n)	Composition (wt%/weigth$_{Filler}$)
SiO_2@APTES	5.48	2.36	15	–	2.31
SiO_2@PEG$_{750}$	8.25	3.39	11	9	3.21
SiO_2@APTES	5.35	2.19	14	–	2.14
SiO_2@PEG$_{5k}$	8.83	4.66	2	40	4.37

were characterized by a negative potential (−25 ± 5 mV), correlated to the presence of surface hydroxide groups.[28] As for the SiO_2@APTES samples (Figure 1a-ii), this value increased until it settled around zero due to the exposure of surface NH_2 groups that reduced the negative charge of pristine silica. Indeed, this analysis is challenging due to the tendency to aggregation/agglomeration in water of hybrid NPs due to the almost zero charge. The ζ-potential increased further when moving to SiO_2@PEG$_{750}$ (21 ± 4 mV) and SiO_2@PEG$_{5k}$ (9 ± 2 mV), which provided a qualitative indication of the change in the surface properties of the particles due to the functionalization.

The amorphous nature of SiO_2@PEG$_X$ was checked by XRD (Figure 1c), where a broad peak characteristic of amorphous silica located at $2\theta = 23°$ [33] both in the pristine silica sample, and after functionalization with APTES and PEG$_x$. Thus, the silica core was left unaltered during the functionalization steps, as also endorsed by TEM and SEM analyses. Figure 1e-i shows the TEM images of the pristine silica NPs. The synthesis procedure led to the formation of spherical nanospheres with an average diameter of 60 ± 7 nm (Figure S2, Supporting Information). DLS analyses on SiO_2 sample (Figure S3, Supporting Information) confirmed the presence of a monodispersed NPs distribution, with a single peak centered at 75 ± 16 nm. The 25% diameter increase was due to the presence of the aqueous solvation sphere around the NPs, as DLS measures the hydrodynamic radius.[34] After the functionalization with PEG$_x$, TEM images showed the appearance of a halo around the NPs corresponding to the thin organic layer which makes the NPs' boundaries less sharp (Figure 1e-ii). The organic functionalization in SiO_2@PEG$_x$ samples was also checked by SEM-EDX analysis (Figure S4, Supporting Information), where the peak related to carbon is visible, which can only be explained by the presence of polymer chains, further evidence of the successful surface functionalization of the NPs.

Finally, the number of APTES and PEG$_x$ chains on SiO_2 NPs was quantified by TGA (Figure 1f). The weight loss referred to the SiO_2 sample was due only to OH groups decomposition and n_{OH} could be estimated with Equation S1 (Supporting Information), which led to an average result of 6.0 mmol g^{-1}. The ^{29}Si MAS-NMR spectra of the two pegylated fillers were similar (Figure 1d).The spectra deconvolution gave Q3 and Q4 moieties with Q3/Q4 ratio of 35%/65%. The Qn notation refers to the [Si(OSi)$_n$(OH)$_{n\text{-}x}$] moieties with 0 ≤ n, x ≤ 4. It must be stressed that not all the Q3 moieties corresponded to functional groups but also included the Si-OH surface groups.[35,36]

According to Equations S2–S4 (Supporting Information), the total weight loss between 150–1000 °C ($\Delta W_{150\text{-}1000}$) was used to calculate the total amount of functionalizing agent (both APTES and PEG, wt%), reaction yield (%), the APTES/PEG effective molar ratios and the composition (wt%), summarized in **Table 1**.[29,37,38] First, the weight loss of SiO_2@APTES is greater than pristine silica, consistently with the introduction of silane molecules on the NPs surface. In parallel, the weight loss of the SiO_2@PEG$_X$ is higher than that of SiO_2@APTES, which confirms the successful functionalization with PEG$_X$ chains. The functionalization with APTES was reproducible with reaction yields ≈15%, which are comparable with literature results.[28] By looking at the APTES/PEG molar ratios, it is evident that the greater steric bulk of PEG$_{5K}$ limited the grafting of PEG compared to the shorter chains of PEG$_{750}$, in agreement with the yield's trend too.

To further evaluate the effective yield of PEG$_X$ grafting, it is possible to use the relationship between the spatial occupation around the NPs and their conformation. Let's consider the Flory's radius (R_F) described as:

$$R_F = \alpha N^{0.6} \tag{1}$$

with $\alpha = 0.358$ nm (PEG monomer length) and N as the number of monomeric units per polymeric chain. The mean distance between two polymeric anchoring points (D) on the NP's surface is given by:

$$D = \sqrt{\frac{4}{\pi d_g}} \tag{2}$$

where d_g is the value of surface grafting density, calculated considering the number of grafted chains and the surface area estimated from the diameter of NPs. This last value for SiO_2@PEG$_{750}$ resulted more than four times larger than the longer PEG$_{5K}$, which confirmed the worse coverage density with SiO_2@PEG$_{5k}$, while shorter chains ensured a higher grafting density. From the ratio between R_F and D, the PEG chains conformation is deduced: for $R_F/D < 1$, PEG chains assume a mushroom conformation, for $1 < R_F/D < 2$, a brush one, while if this ratio exceeds 2, the conformation is of a dense brush. The result obtained for SiO_2@PEG$_{750}$ is 1.3, while for SiO_2@PEG$_{5k}$ is 1.8, indicating for both the hybrid fillers a brush regime with high grafting density and a satisfying covering.[39–41]

Thus, considering the reported analysis, it is possible to conclude that the functionalized nanoparticles were successfully

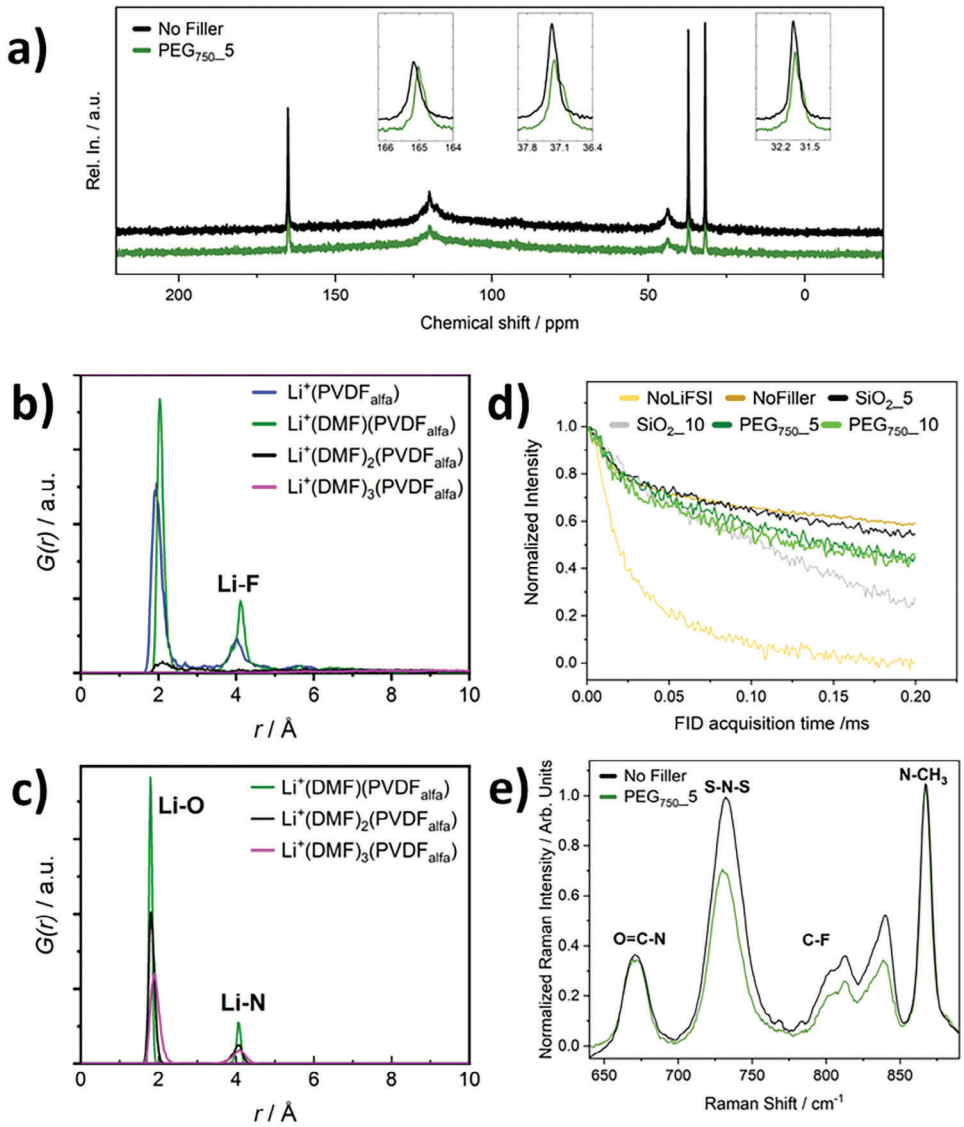

Figure 2. a) ^{13}C MAS-NMR spectra of PEG_{750}–5 compared to the membrane without filler, with inserts to better show the more interesting regions; b) DFT-simulated Pair Distribution Function (PDF) between Li and F atoms of $Li(DMF)_n(PVDF)^+$ (n = 0–3); c) PDF between Li and O/N atoms of $Li(DMF)_n(PVDF)^+$ (n = 1-3); d) NMR Free Induction Decays (FIDs) of the membranes, acquired at low field using the Multiple Spin Echo (MSE) sequence at 40 °C. For reference, the fast-relaxing reference polymer membrane without LiFSI is also shown; e) Raman spectra of sample PEG_{750}–5 and for the sample without filler. Spectra are normalized to the $N\text{-}CH_3$ symmetric stretching of the solvent.

prepared. They are characterized by an average diameter of 60 ± 7 nm and a functionalization of 3.21% wt for PEG_{750} and of 4.37% wt for PEG_{5k}, respectively.

2.2. QSE Membrane: Host-Guest Interactions and the Role of the Filler

Different contents of the synthesized fillers (SiO_2@PEG_{750}, SiO_2@PEG_{5K} and pristine SiO_2 for comparison) were added to PVDF-HFP/LiFSI polymer matrix to obtain self-standing membranes, with the compositions listed in the Experimental Section. Filler contents in the range 5–15 wt% with respect to the membrane weight were investigated. As an example, the name PEG_{750}–5 indicates a membrane with 5 wt% of filler grafted with PEG_{750}.

First, the membranes were characterized with ^{13}C MAS-NMR to address the interactions of the filler with the polymer matrix and the residual DMF solvent. **Figure 2a** shows the comparison between the reference membrane without filler and the membrane PEG_{750}–5. The spectra of two samples are nearly superimposable for all the signals. The signals of the PVDF-HFP backbone (120 ppm region) are unaltered in position and broadening, similarly the extra signals were attributed only to the DMF solvent (sharp resonances at 32, 37, 165 ppm),[25] whereas no evidence of THF trapping was observed. A detailed discussion of such a system was reported in the companion paper.[25] While the signals of the polymer were essentially superimposable for the two

samples, the signals of the DMF moieties were slightly modified by the presence of the filler, as highlighted from the inserts in Figure 2a. Indeed, the DMF signals of carbonyl (165 ppm) and -CH_3 (37 ppm) were shifted upfield (increasing electron shielding) and appeared to be structured, leading to at least two contributions, which could be assigned to the existence of populations differently affected by the filler. Smaller effects were observed for the -CH_3 at 32 ppm. As the NMR spectra were obtained with high-power ^1H decoupling, quantitative determination of the polymer/solvent ratio could be performed. The polymer/solvent ratio can be estimated 77:23 wt.%:wt.% for the membrane without filler and 74:26 wt.%:wt.% for the other one. Thus, the effect of the filler can be rationalized into helping the retaining of the solvent into the membrane also after the drying period. Retained solvent fractions higher than 20 wt.% must be expected in case of mild drying procedures.[25]

Figure 2d shows the NMR Free Induction Decays (FIDs) acquired with the Multiple Spin Echo (MSE) sequence at 40 °C, which is representative of realistic work conditions. As expected, the polymer on its own is very stiff, and the FID is represented predominantly by a fast Gaussian decay. By adding the salt, and possibly due to the plasticizing effect of DMF that was retained in the sample, the system became much softer, represented by a slow relaxing FID with a small initial Gaussian component, ≈23% of the total, possibly associated to crystalline regions or rigid amorphous fractions. With 5% bare SiO_2 particles, the FID remained identical, as if the NPs were dispersed without interacting with the matrix. Instead, by using the same amount of PEG_{750}-grafted NPs, the mobility of the more mobile regions decreased, indicating an interaction between the PEG_{750} chains and the polymer matrix. Interestingly, by increasing the content of functionalized NPs there were no relevant changes, while 10% of SiO_2 NPs caused a massive decrease in the mobility of the matrix. Indeed, a small amount of SiO_2 could be tolerated basically as a non-interacting inclusion, while a larger amount totally disrupted the polymer matrix. Instead, SiO_2@PEG_{750} blended smoothly in the matrix, likely due to the SiO_2 functionalization.

More detailed and complementary information on the filler role was obtained by Raman spectroscopy measurements performed on the same samples. The spectra in the region of interest from 615 to 890 cm^{-1} were reported in Figure 2e, while full spectra are reported in the Figure S5a,b (Supporting Information). Indeed, the vibrational modes most indicative of solvent, polymer and anion geometry fall in this spectral region. Specifically, peaks at 672 and 867 cm^{-1} corresponded to O = C-N bending ($\delta_{O=C\text{-}N}$) and N-CH_3 symmetric stretching ($\nu_{N\text{-}CH3}$) of DMF molecules.[42] The peak occurring at 730 cm^{-1} was originated by the S-N-S symmetric stretching of FSI anion ($\nu_{S\text{-}N\text{-}S}$) molecules.[43] Lastly, the group of bands in the region 780–820 cm^{-1} were assigned to C-F side chain stretching modes of the guest polymer.[44] Spectra were normalized with respect to the solvent $\nu_{N\text{-}CH3}$ peak. The relative intensities of bands associated to anion and polymer were lower for the sample containing the filler. This result indicated, in agreement with the NMR results, that the filler retained more solvent during the drying process than the unfilled reference sample. Closer examination of the shape and position of the peaks showed that the presence of the filler had no drastic effects on the membrane components, but some minor changes in solvation could be argued by detailed analysis. As regard the solvent, the most indicative peak about solvation is the $\delta_{O=C\text{-}N}$,[45,46] while for the anion is the $\nu_{S\text{-}N\text{-}S}$.[47] $\delta_{O=C\text{-}N}$ is identical in both samples in terms of width and position. In both cases, the peak fell ≈13 cm^{-1} further away than the pure DMF peak taken in the same experimental conditions. This shift toward higher wavenumbers is symptomatic of the presence of bound DMF species with a relatively low population of free solvent molecules.[25] However, the nature of the species interacting with the solvent in this bound conformation couldn't be resolved by Raman spectroscopy. The $\nu_{S\text{-}N\text{-}S}$ peak, instead, showed some small, but significant, difference between the two samples. This peak can be described by the sum of three Gaussian functions with centers at 719, 731, and 739 cm^{-1}. The three peaks were associated with the stretching mode of the anion in the free, contact ion pair (CIP, where one FSI^- interacts with one Li^+) and aggregate (AGG, where one FSI^- interacts with at least two Li^+) geometries, and the areas of these peaks directly correlate with their respective populations.[25,47–49] For both samples, free anion species were not detected and the solvation was entirely due to the CIP and AGG configurations (see Figure S5c,d; Table S1, Supporting Information).

The interaction between Li^+ and DMF in the PVDF-based matrix was analyzed by DFT calculations. We found that Li^+ interacts preferentially with DMF, while its interaction with the PVDF chains is weaker or even negligible.[25] We also studied the interaction of Li^+ with a triglyme as a model for PEG_x, and found a binding energy of −0.80 eV (see Figure S6 and Table S2, Supporting Information), which is stronger than the binding energy of $Li(DMF)^+$ (−0.67 eV), but weaker than the interaction with two or three DMF (−1.32 eV for $Li(DMF)_2^+$ and −1.91 eV for $Li(DMF)_3^+$, Table S2, Supporting Information),[25] indicating that Li^+ preferentially coordinates with multiple DMF molecules if there is enough residual DMF in the electrolyte. Given this result and the relative low concentration of SiO_2@PEG_x in our experiments (see Experimental Section), we did not consider the functionalized SiO_2@PEG_x filler in our model when simulating Li-ion diffusion by *Ab-initio* Molecular Dynamics (AIMD). We propagated the trajectories of Li^+ and $Li(DMF)_n^+$ (n = 1-3) in the vicinity of a PVDF chain for 30 ps after 5 ps of equilibration at 350 K. Figure 2b reports the calculated Pair Distribution Function (PDF) between Li and F atoms of $Li(DMF)_n(PVDF)^+$. Starting from the $Li(PVDF)^+$ system, we observed that the cation interacts on average with three fluorine atoms (Table S3a, Supporting Information) with a distance of 1.93 Å (Figure S7a, Supporting Information). The addition of a single DMF molecule in the $Li(DMF)(PVDF)^+$ system led to a weakening of the Li-F interaction as evinced by an elongation of the average bond length, from 1.93 to 2.03 Å. Nevertheless, the coordination number was three in both cases, indicating that the introduction of one DMF molecule did not imply any bond breaking between Li and F, as also evident in a representative snapshot in Figure S7b (Supporting Information). The picture changed when more than a single DMF was present. Indeed, the coordination number between Li and F dropped to 0.3 only for $Li(DMF)_2(PVDF)^+$ (see Table S3 and Figure S7c, Supporting Information), indicating that the interaction with PVDF was strongly weakened. Also, the averaged Li-F distance was longer than the previous cases, 2.12 Å. When looking at $Li(DMF)_3(PVDF)^+$, we did not detect any interaction with PVDF, while the cation was coordinated by DMF only and it moved around as a single entity (see Figure S7d, Supporting

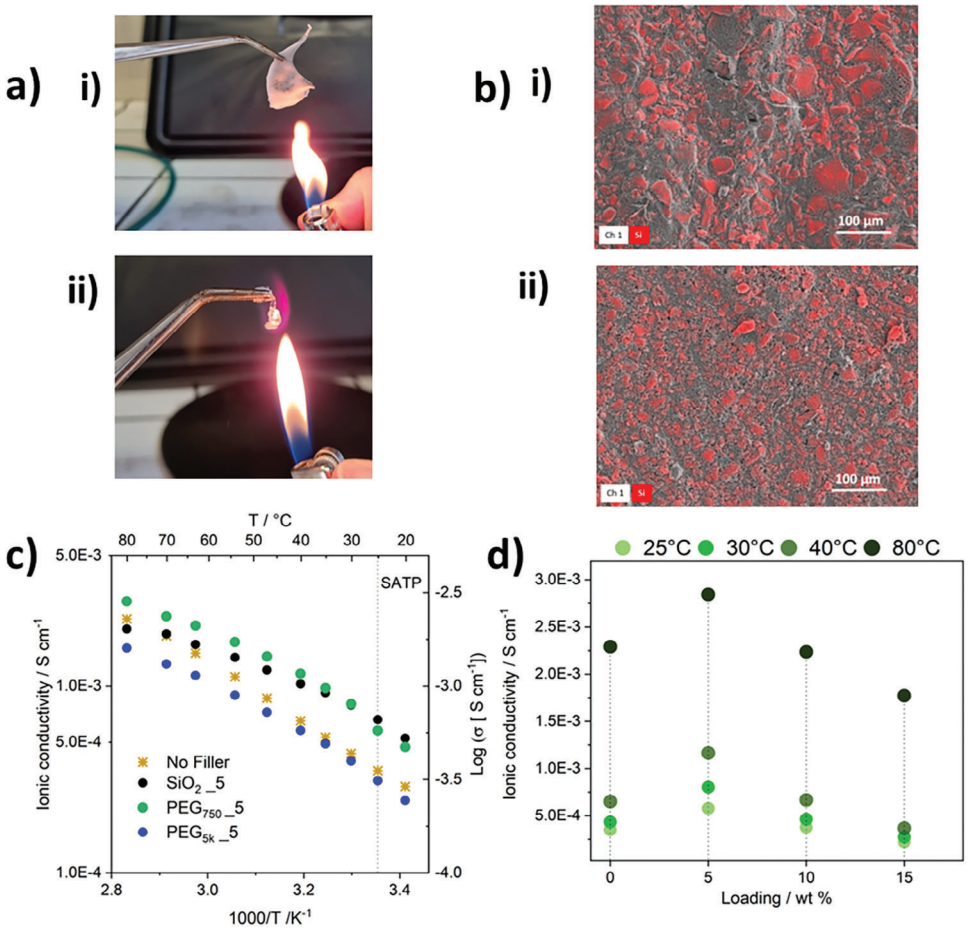

Figure 3. a) Flammability test comparing the stability of PEG_{750}–5 electrolyte exposed to a free flame for ten seconds (i), to the instability of a Celgard 2400 separator soaked in a solution of LiFSI-DMF (1:2 mol) (ii); b) SEM-EDX images evidencing the silicon (red) less homogeneous dispersion in SiO_2–5 (i) than in PEG_{750}–5 (ii) membrane; c) ionic conductivity Arrhenius plots of nanocomposite electrolytes (loading of filler: 5 wt.%) compared to the membrane without filler; d) ionic conductivity values versus loading of SiO_2@PEG_{750} at four different temperatures.

Information). **Figure** 3c shows the PDFs between Li and O(N) atoms of DMF. Clearly, Li^+ prefers to bind O species than N ones, as evidenced by the shorter Li-O distances. When increasing the number of DMF molecules up to three, the coordination number increased from 1 to 2.98, further demonstrating the tendency of Li^+ to bind three DMF molecules at the same time (see Table S3b and c, Supporting Information). The interaction between Li^+ and the DMF molecules is quite strong since the distance with the nearest neighboring atoms was unchanged in $Li(DMF)_n(PVDF)^+$ with n = 1,3, although the distance distributions became larger with increasing the number of DMF molecules coordinating Li^+.

2.3. QSE Membrane: Physico-Chemical and Transport Properties

The TGA curve in Figure S8 (Supporting Information) shows the weight loss of the composite electrolyte membrane compared to a membrane without filler 14 days after preparation, during which the membranes were stored in closed vials without any special precaution to prevent them from being exposed to air. Whereas we could not derive reliable quantitative information on the fraction of trapped solvent due to the degradation of the salt-polymer system,[25] we could appreciate how the composite membrane exhibited a greater weight loss in the region around the boiling point of DMF (153 °C), revealing a higher retention of the polar solvent within the polymer structure during preparation, that was also retained over time.

A key feature of a solid electrolyte is lower flammability than commercially used liquid ones to increase safety during both assembly and use of the final device. This was preliminary evaluated through exposition to a free flame for 10 s. The PEG_{750}–5 membrane was thermally stable under this extreme condition, not catching fire, differently from a commercial Celgard separator soaked in a solution of DMF and LiFSI, which caught fire immediately due to the presence of free solvent (Figure 3a).

The membranes were analyzed with SEM-EDX to investigate the surface morphology and elemental distribution (Figure 3b). In the SiO_2–5 sample, an inhomogeneous distribution of silicon is visible. Conversely, in the PEG_{750}–5 membrane the NPs were homogeneously distributed within the matrix, likely due to the chemical compatibilization offered by the polymer chains grafted onto the NPs' surface. This also influenced the ionic

conductivity. Figure 3c shows the Arrhenius plots of the membranes containing 5 wt.% of the different fillers compared with the membrane without filler (No Filler). The parameters of the Arrhenius fits are reported in Table S4 (Supporting Information). For the membranes with low filler content a fit with the VTF equation seemed more appropriate (the VTF fit of PEG_{750}–5 is reported in Figure S9 as an example, Supporting Information). VTF behaviors are generally associated with the existence of available free volume, which can be expected in case of gel polymer electrolytes.[50] Whereas the systems under study cannot be considered as real "gels", the residual DMF in the matrix allows the formation of gel-like structure. The addition of filler, indeed, led to a reduction of the free volume, making more Arrhenius-like the ionic conductivity behavior. Figure 3c shows that the addition of filler determined the increase of ionic conductivity with respect to the pure electrolyte membrane, but for the SiO_2@PEG_{5k}. The highest conductivity values were obtained with the SiO_2@PEG_{750} filler, even if at 25 °C the membrane with 5 wt.% of pristine silica scored better. It is interesting to observe (see Figure S10a,b, Supporting Information) that, at higher loading values (10 wt.% and 15 wt.%), surface functionalization with PEG_x still resulted in a marked improvement in ionic conductivity compared to the membrane with pristine silica alone, probably due to the increased compatibilization with the matrix allowing for better dispersion of NPs. Figure 3d shows the relationship between the weight of SiO_2@PEG_{750} filler and the ionic conductivity at four different temperatures. At the room temperature, a maximum of ≈0.7 S cm^{-1} was observed for 5 wt.%, which is well aligned with values in the range 0.1÷1 S cm^{-1} already reported for similar PVDF-HFP-based composite membranes.[51] This conductivity maximum is likely due to the onset of an interface transport mechanism like that already discussed for PEO-based electrolytes.[52] More than to the increase in the number of charge carriers, the increase in conductivity due to the filler is due to the increase in the mobility of lithium ions. In fact, the presence of 5 wt.% filler causes an increase in the spin-lattice relaxation time (T_1) obtained from solid state ^{7}Li NMR, which goes from 320 ms for the reference membrane to 445 ms for the PEG_{750}–5 sample. The longer T_1, the weaker the cation-lattice interactions. Increasing filler amount led to a conductivity decrease because of dilution effects.[53,54] Figure S11 (Supporting Information) showed that longer PEG chains gave worse ionic conductivity compared to the system without filler, likely because of the low grafting density of PEG_{5k} which reduced the compatibility between the filler and the polymer strands. The electrical conductivity was estimated to 9 ± 1 10^{-12} S cm^{-1} at room temperature (see Figure S12, Supporting Information), confirming the expected negligible contribution of electrons and holes to the total conductivity which appears dominated by ion migration.

The mechanical properties of the membranes were then measured by means of tensile tests to investigate the filler-reinforcing effect (**Table 2**). The pure PVDF-HFP membrane showed a higher tensile modulus (E_T) compared to all the other membranes due to the absence of LiFSI, that acts as a plasticizer with a sharp decrease of the tensile modulus.[55]

The QSE without filler showed E_T = 18.9 ± 3.6 MPa, like that reported for sulphonated PVDF-HFP membranes.[56] Interestingly, the addition of fillers (both pure and functionalized) causes a generalized worsening of tensile modulus and maximum load with respect to the No Filler sample. On the other hand, E_T values in the range 1÷10 MPa are usually reported for composite PVDF-HFP QSEs.[51] However, we noticed a partial restoring of the mechanical properties by increasing the amount of NPs, especially for the functionalized ones. This confirms a positive interaction of the PEG chains with the matrix polymer strands.[57,58] The same effect was observed for the maximum load.

Table 2. Mechanical properties of some selected samples. E_T = tensile modulus; σ_M = maximum load.

Sample	E_T (Mpa)	σ_M (Mpa)
PVDF-HFP	271.0 ± 37.3	13.4 ± 0.7
No Filler	18.9 ± 3.6	2.65 ± 0.29
SiO_2–5	12.3 ± 4.3	2.26 ± 0.20
SiO_2–10	13.5 ±2.8	2.35 ± 0.61
PEG_{750}–5	14.3 ± 2.5	2.55 ± 0.37
PEG_{750}–10	16.2 ± 1.7	2.68 ± 0.58

2.4. QSE Membrane: Functional Properties

Finally, we investigated the electrochemical properties of the PEG_{750}–5 compared with the reference (No Filler) membrane. **Figure 4a** shows the membranes stability range: both the reference membrane and the PEG_{750}–5 one were stable in oxidation up to 4.5 V versus Li^+/Li, thus being compatible with most currently used cathode materials. Also, the filler increased the stability window of about 0.25 V. Besides, the oxidation potential remained unchanged with cycling (Figure 4b), which confirmed the ability of the composite electrolyte (PEG_{750}–5) to allow reversible stripping and plating. Moreover, no reductive peaks attributable to degradative phenomena, that could result in system instability, were visible at low potentials.

The electrolytes with 5 wt.% of the different fillers, showing the best ionic conductivity values, were tested into symmetric Li/Li cells to evaluate their resistance against dendrite penetration at 30 °C (Figure 4c). The membrane without filler exhibited limited performance and underwent short-circuit after a modest number of cycles, demonstrating a sharp worsening of the interfaces. The nanocomposite membranes offered significantly better results, especially in the case of PEG_{750}–5, which not only sustained the entire test up to 500 μA cm^{-2} without showing significative differences between the last step and the second one at 100 μA cm^{-2} but confirmed its excellent stability at 100 μA cm^{-2} for a total of 250 operating hours (see Figure 4d). The addition of hybrid organic-inorganic filler led to more robust membranes, resistant to penetration of lithium dendritic structures, which would lead to premature cell failure during analysis.

The most promising sample was tested in a lithium metal battery with an LFP-based cathode to verify its real behavior (Figure 4e). PEG_{750}–5 was cycled in a climatic chamber at 30 °C at a current rate of 0.1C (17.7 μA cm^{-2}) to test its stability and functioning with a cathodic material in a coin cell. It gave stable performance for more than 100 cycles, with a high mean discharge capacity (99.7 mAh g^{-1}), a mean Coulombic Efficiency (CE) after the second cycle of 99.14%, and a plateau at 3.43 V, value that fits exactly with the expected.[59] These results are even more

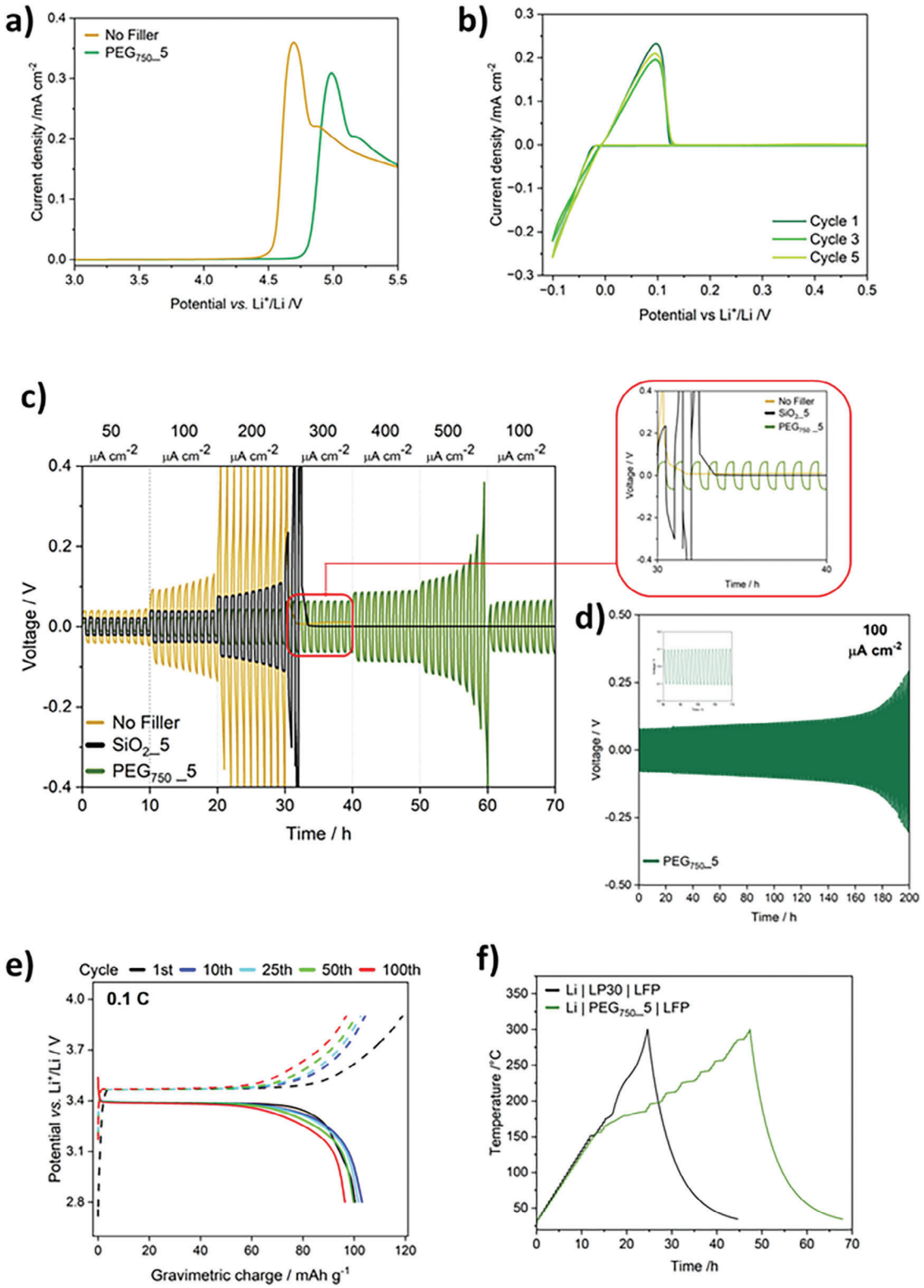

Figure 4. a) LSV curves of PEG_{750}–5 compared to the No Filler membrane, evidencing the improved stability range in oxidation; b) CV curves of PEG_{750}–5, shown in the potential range from −0.100 V to 1.00 V versus Li^+/Li; c) comparison between stripping-plating analyses at different current densities performed on the membrane without filler, SiO_2–5 and PEG_{750}–5, with the evidenced region in which short circuits happen; d) continuous stripping-plating measurement at 100 µA cm^{-2} on the previously cycled PEG_{750}–5, with an inset which better shown the regular profile of the graph; e) charge/discharge profiles of Li | PEG_{750}–5 | LFP full cell operating at 30 °C; f) ARC profile of the fully charged Li | PEG_{750}–5 | LFP full cell compared to the twin reference one with the commercial electrolyte LP30.

remarkable if compared with the same cell Li | LFP with the reference electrolyte membrane without filler (Figure S13, Supporting Information), that proved to be inefficient and incapable of cycling already from the very first cycles, with a mean discharge capacity of 38.5 mAh g^{-1} considering the first ten cycles.

Accelerated Rate Calorimetry (ARC) was used to investigate the thermal behavior of the Li | PEG_{750}_5 | LFP cell fully charged at 0.1C, compared to a twin cell with a commercial electrolyte (Whatman separator with $LiPF_6$ (1 M) in EC:DMC 1:1 vol/vol). The working principle and chosen parameters are schematically represented for clarity in Figure S14 (Supporting Information). In general, LFP is a cathode material which shows high stability under thermal abuse.[60] Differently from the cell realized with the commercially available liquid electrolyte, which underwent a thermal runaway ≈175 °C, the nanocomposite membrane did not show any thermal runaway up to 300 °C (Figure 4f), so demonstrating a superior cell safety.

3. Conclusions

In this paper, we prepared and thoroughly characterized nanocomposite QSE membranes with functionalized SiO_2-based nanofillers. We showed that PEG_x grafting on silica NPs ensures multiple benefits: on one hand, it allows obtaining a better filler dispersion (in case of short polymer chains) by increasing its chemical compatibility with the polymeric matrix. On the other hand, it allows to increase the ionic conductivity, thanks to a conduction mechanism encompassing the formation of pathways with increased Li^+ mobility, in addition to the DMF-assisted Li^+ transport in the fluorinated polymer matrix.

We showed that nanocomposite PVDF-HFP membranes synthesized by a simple solvent-casting method can provide adequate mechanical reinforcement against dendrite perforation, excellent chemical and electrochemical stability, good ionic conductivity, and promising performance in LMBs. At the same time, due to their semi-solid nature, they reduce the issues of toxicity and solvent flammability that make unsafe the liquid electrolytes commonly used in commercial batteries.

4. Experimental Section

Materials: *Hybrid silica NPs* Tetraethyl orthosilicate (TEOS, 98%) and ammonium hydroxide solution (NH_4OH, 25 wt%) were purchased from Sigma-Aldrich, while ethanol absolute (EtOH), toluene (99%) and Milli-Q water were purchased from VWR Chemicals. (3-aminopropyl) triethoxysilane (APTES, 98%) and succinic anhydride (SA, 99%) were purchased from Alfa Aesar. Poly(ethylene glycol) methyl ether (PEG_{750}, Mw = 750 g mol^{-1} and PEG_{5k}, MW = 5000 g mol^{-1}), dichloromethane (DCM, ≥99.8%) and triethylamine (Et_3N, ≥99%) were purchased from Sigma–Aldrich. All the chemicals were used as received.

QSEs N,N-dimethylformamide (DMF, 99.8%, anhydrous) and tetrahydrofuran (THF, 99.8%, anhydrous) were purchased from Alfa Aesar, while lithium bis(fluorosulfonyl)imide (LiFSI, 99.9%) was purchased from Solvionic. Poly(vinylidene fluoride-co-hexafluoropropylene) (PVDF-HFP Kynar 2751) was obtained by Arkema, and vacuum heated at 100 °C overnight before using it.

LFP Cathode LFP powder was obtained from Hydro-Quèbec. The X-ray diffraction pattern and the SEM image of LFP were reported in Figures S15,S16 (Supporting Information), respectively. Super P carbon black from Sigma-Aldrich while PVDF (Solef 6010), used as binder, was acquired from Solvay.

Synthesis of Hybrid Silica NPs: The synthetic procedure is fully illustrated in Figure 1a. It consists of four steps, the products of which are marked with lowercase letters in the illustration (a-d). First, pristine silica NPs (Figure 1a-i) were prepared through the Stöber method, a sol-gel approach that ensures good dimensional control uniformity.[61] In a typical preparation, 10.81 mL of Milli-Q water and 1.529 mL of NH_4OH were added in a 250 ml round-bottom flask containing 100 mL of EtOH at room temperature (RT). After 10 min, 6.245 mL of TEOS were added and the solution was stirred at 550 rpm at RT for 23 h. The so-obtained NPs were collected through centrifugation (9000 rpm for 30 min) and washed twice with 10 mL of EtOH, and an additional time with 10 mL of Milli-Q water. Then, SiO_2 NPs were dried overnight at 75 °C.

Subsequently, pristine SiO_2 NPs were functionalized with APTES. Thus, 1.0 g of SiO_2 were dispersed in 24 mL of EtOH with 100 µL of NH_4OH (25%), at 600 rpm for 15 min at 80 °C, and APTES was added; the amount of APTES used is chosen to have a molar ratio between APTES and the surface OH groups on silica (n_{OH}) equal to 1:2, where n_{OH} was calculated from thermogravimetric analysis (TGA) based protocols and specifically according to Equation S1 of the Supporting Information, and was equal to 6.0 mmol g^{-1}.[29,62] After 24 h, the product (SiO_2@APTES, Figure 1a-ii) was centrifuged, washed twice with EtOH and dried overnight at 75 °C.

The PEG_x chains were activated as follows: 2.50 g of PEG_x were added to 8 mL of DCM with a quantity of SA chosen to have a molar ratio between PEG_x and SA equal to 1:1. 10 µL of Et_3N were used to catalyse the reaction with PEG_{5k}, while 50 µl were required with PEG_{750}, due to the higher quantity of chains for the same polymeric mass used. The mixture was then vigorously stirred in a closed round-bottomed flask at reflux (50 °C) for 8 h and the product (PEG_X-COOH, Figure 1a-iii) was isolated by rotary evaporation.

The last step consisted in PEG_x-COOH grafting on SiO_2@APTES thanks to the interaction between the APTES amino groups and PEG carboxylic units.[28] 0.80 g of SiO_2@APTES were added in 24 mL of toluene at 100 °C with a suitable amount of PEG_x-COOH, to have a molar ratio between amino groups (n_{APTES}, calculated from TGA according to Equation S2, Supporting Information) and PEG_x equal to 2:1 for PEG_{5k}-COOH, and 1:1 for PEG_{750}-COOH. In the latter case, the aim was to bind as many chains of PEG_{750} as possible on the NPs surface, taking advantage of the lower steric bulk compared to PEG_{5K}. After 22 h, the mixture was centrifuged and washed twice with toluene. The resulting pegylated powder (SiO_2@PEG_x, Figure 1a-iv) was left to dry overnight at 75 °C to be finally used as the filler.

Fabrication of QSEs: The membranes were prepared by solvent-casting method inside an Ar-filled glove box (MBraun, H_2O, O_2 < 0.1 ppm) to ensure the solvent evaporation in a controlled atmosphere. PVDF-HFP and LiFSI (mass ratio 3:2) were dissolved in a binary solvent (DMF:THF, 3:7 vol/vol) to obtain a concentration of 7.50 wt.%, that ensures a total solutes' dissolution and a proper viscosity. Then, a proper amount of filler (5, 10, 15 wt.%) was added to the mixture, which was then dispersed under mechanical stirring at room temperature and poured onto a circular PTFE mould. After 72 h at room temperature, the membrane was detached and used for successive measurements. The resulting thickness was measured using a screw gauge micrometer (sensitivity ±10 µm). All the prepared compositions are reported in **Table 3**.

Characterizations: *Chemical-physical analysis*: The pristine silica NPs were morphologically characterized with Transmission Electron Microscopy (TEM, JEOL JEM 2100 Plus) and Dynamic Light Scattering (DLS, Malvern Zetasizer Nano Series ZS90), also employed to determine the ζ-potential; the samples were diluted in milli-Q H_2O (≈0.1 mg mL^{-1}) at RT. All the synthesized products (a-d) were structurally investigated by X-ray powder Diffraction (XRD), using a Rigaku Miniflex 600 equipped with a Cu source (1.54 Å) in the 2θ range of 10–60°, with a scan rate of 1°min^{-1}. The surface characterization was carried out by Fourier Transformed Infrared (FTIR) spectroscopy in the Attenuated Total Reflectance (ATR) mode on a Thermo Fisher Scientific Nicolet iS20 instrument, in the wavenumber range 4000–500 cm^{-1} (resolution spectra 4 cm^{-1}, 32 scans).

Surface functionalization of SiO_2@PEG_x was investigated through Scanning Electron Microscopy with Energy Dispersive X-ray Analysis (SEM-EDX), using a Zeiss Gemini 500 equipped with a Bruker

Table 3. Nominal composition of QSEs, with an indication of the name used in the text, the percentage content of polymer matrix (PVDF-HFP), salt (LiFSI), silica and PEG_x grafted on the hybrid NPs, if present. The thickness was obtained as a mean value among all the samples (>3) realized with the same composition.

Sample	SiO_2 (wt.%)	LiFSI (wt.%)	PVDF-HFP (wt.%)	Grafted PEG_x (wt.%)	Thickness (µm)
Pure polymer	0	0	100	0	118 ± 12
NoFiller	0	40.0	60.0	0	165 ± 7
SiO_2_5	5.1	38.1	56.8	0	95 ± 21
SiO_2_10	10.2	36.0	53.8	0	160 ± 6
SiO_2_15	15.2	34.0	50.8	0	120 ± 9
PEG_{5k}_5	5.1	37.8	56.5	0.2	150 ± 5
PEG_{5k}_10	10.0	35.5	53.4	0.5	130 ± 38
PEG_{5k}_15	15.0	33.4	49.9	0.7	180 ± 12
PEG_{750}_5	5.2	37.8	56.8	0.2	170 ± 21
PEG_{750}_10	9.9	35.9	53.8	0.3	156 ± 32
PEG_{750}_15	15.0	33.7	50.4	0.5	200 ± 15

QuantaX-Ray detector. For SEM analyses the samples were previously sputter-coated with a thin layer of gold. The same analysis was conducted on the nanocomposite membranes.

NPs thermal properties and the quantification of functionalizing agents onto the hybrid filler were finally studied with the Thermogravimetric Analysis (TGA) with a Star System Mettler Toledo, in a temperature range 30–1000 °C, heating rate of 10 °C min^{-1} under constant air flux of 50 ml min^{-1}. The heating method involved heating the sample from 30 °C until it reached 150 °C, a temperature that was kept constant for 10 min. This isotherm made possible to accurately distinguish weight losses related to species covalently attached to the NPs surface from those that were simply physi-sorbed (e.g., solvent molecules), which detached already at lower temperatures, and whose contribution did not affect the results.

The mechanical properties of the membranes were characterized by performing tensile tests at room temperature on a ZwickRoell RetroLineTesting Machine, considering the mean value obtained on 5 rectangular specimens, with preloading of 0.01 N and a traction rate of 100 mm min^{-1}. Then, the amount of entrapped DMF solvent was measured by TGA, heating from 30 to 250 °C, at heating rate of 10 °C min^{-1} under constant nitrogen flux of 50 ml min^{-1}.

NMR Characterization: Solid-state Nuclear Magnetic Resonance (NMR) measurements were performed using an Avance III Bruker spectrometer 400 MHz, equipped with a 4 mm Magic Angle Spinning (MAS) probe for ^{13}C and ^{7}Li acquisitions (rotation frequency 10 kHz) and with a 7 mm MAS probe (rotation frequency 5 kHz) for ^{29}Si acquisitions. ^{13}C spectra were acquired with high power decoupling under MAS conditions with 1k scans, 90° pulse of 4 µs, delay time of 50 s and referenced to adamantane signal as secondary standard. ^{29}Si spectra were acquired with one pulse acquisition sequence, 90° pulse of 10 µs, 8 k scans and 50 s delay time. The spectra were referenced to tetramethylsilane (TMS, 0 ppm) under MAS conditions. ^{7}Li spectra were collected with one-pulse sequence with 128 scans, 90° pulse of 4.5 µs, delay time of 5 s, and reference to LiCl aqueous 1 M signal. The ^{7}Li NMR Spin-lattice relaxation time, T_1, was determined under static (i.e., not MAS) conditions using a standard Inversion-Recovery sequence.

The local mobility of polymer chains was investigated by ^{1}H Time Domain NMR (TD-NMR). For each relevant sample, an aliquot of ≈100 mg was inserted in a 10 mm NMR tube. The rigid fraction of the samples was quantified using the MSE pulse sequence, with 2 s recycle delay and a large number of repetitions since the total proton content was very low in the highly fluorinated polymer system. The instrument used for the analysis is a Bruker Minispec mq20, equipped with gaseous nitrogen BVT3000 heating unit.

Density Functional Theory Calculations: Density functional theory (DFT) in conjunction with *Ab-initio* molecular dynamics (AIMD) computations as implemented in the VASP package[63] to analyze the diffusion of $Li(DMF)^{+}_{n}$ (n = 1–3) in a PVDF matrix was performed. The generalized gradient approximation of the exchange and correlation functional with the Perdew–Burke–Ernzerhof (PBE) formalism was used.[64] The valence electrons were treated explicitly and expanded on a set of plane waves with a kinetic cutoff of 400 eV, whereas the core electrons were treated with the projector augmented wave approach (PAW).[65] AIMD trajectories were propagated for 30 ps after 5 ps of equilibration. This propagation time allows to provide reasonable results on the nature of the interaction between different species.[66,67] The temperature was set to 350 K and was controlled by a Nose-Hoover thermostat.[68,69] For the sake of simplicity, pure PVDF was used as the polymer matrix instead of PVFD-HFP, provided that Kynar 2751 is just 6 mol% of HFP. We modelled a PVDF chain in the α-conformation by creating a working $1 \times 1 \times 2$ supercell containing $C_{16}F_{16}H_{16}$ units. We studied the interaction and diffusion of Li^{+} (one atom per cell) with α-PVDF in the presence of an increasing number of DMF ($n = 1-3$). The nature of the interaction between Li^{+}, the PVDF matrix and DMF was investigated by looking at Pair Distribution Functions (PDFs).[70] The interaction of Li^{+} with triglyme, as a model for PEG_x, has been computed with the Gaussian16 suite[71] at B3LYP/6-31G(d,p) level of theory. Solvation effects were accounted with a conductor-like polarizable continuum model (CPCM)[72,73] with a dielectric constant $\epsilon = 10.2$, close to the one of PVDF ($\varepsilon' \approx 10-11$).

Raman Spectroscopy: Micro-Raman measurements were conducted at room temperature using a LabRAM confocal spectrometer (Horiba Jobin-Yvon) with a He-Ne laser operating at 632.8 nm in a backscattering configuration. The 50x long working distance objective with a numerical aperture of 0.60, mounted on a microscope head (Olympus BX40), was employed to collect the scattered light. A charge-coupled device (CCD-Sincerity, Jobin-Yvon) with a resolution of 1 cm^{-1} detected the scattered light. The spectral position of the detection system was calibrated using the 521 cm^{-1} Raman line of crystalline silicon as a standard, a procedure repeated before each measurement.

Coin Cell Tests: Accelerated Rate Calorimetry (ARC, THT) with a typical "heat-wait-seek (HWS)" mode was applied to Li | LFP cells, heating from 35 to 300 °C with temperature step of 5.00 °C and a sensitivity of 0.02 °C min^{-1}.

The electrochemical measurements were performed with a Biologic VMP3 multichannel potentiostat, while the conductivity analyses were collected with a Biologic SP-150 single channel electrochemical station on symmetric stainless-steel (SS) coin cells in the temperature range from 20 to 80 °C, in the frequency range from 100 Hz to 1 MHz with a fixed wave amplitude of 20 mV. The ionic conductivity (σ) was calculated as:

$$\sigma = \frac{1}{\rho} = \frac{k}{R} \quad (3)$$

where k is the cell constant, expressed in cm^{-1} and defined as is the ratio of membrane thickness to electrode area, and R, expressed in Ohm, was obtained by Electrochemical Impedance Spectroscopy (EIS) measurements by considering the low frequency intercept with x-axis. The activation energies were calculated first in accordance with the Arrhenius equation:

$$\sigma\ (T) = \sigma_0\, e^{-E_{att}/k_B T} \tag{4}$$

where σ_0 and E_{att} are the pre-exponential factor and the activation energy of ion transport expressed in eV, respectively, while k_B was the Boltzmann constant ($8.617 \cdot 10^{-5}$ eV K^{-1}), and according to the Vogel-Tammann-Fulcher (VTF) equation:

$$\sigma\ (T) = \sigma_0\, e^{-\frac{B}{T-T_0}} \tag{5}$$

where B is the activation pseudo-energy, and T_0 is an adjustable parameter.

Electrical conductivity was also measured using asymmetric coin cells with a lithium electrode (diameter 12 mm) and a blocking electrode of stainless steel (diameter 16 mm) sandwiching the membrane PEG_{750}–5 as an exemplificative sample. After having applied a constant potential for a prolonged time (t≥12 h), the steady-state current related to the motion of electron and holes $i_{e,h}$ was obtained. The electronic conductivity $\sigma_e + \sigma_h$, attributable to both electron and holes, was then determined by Hebb-Wagner polarization measurements to further clarify the conductive behavior of this system:[74]

$$i = \frac{kT}{eL}\left[\sigma_e\left(\exp\left(-\frac{Ue}{kT}-1\right)+\sigma_h\left(1-\exp\left(\frac{Ue}{k_B T}\right)\right)\right)\right] \tag{6}$$

$$\sigma_e + \sigma_h = \frac{L}{A}\frac{d\left|i_{e,h}\right|}{dU} \tag{7}$$

where L is the thickness of the electrolyte, A is the contact area, U the applied voltage and e is the electronic charge.

Linear Sweep Voltammetry (LSV) was performed with a scan rate of 0.100 mV s^{-1} from open-circuit voltage (2.3 V) to 5.5 V versus Li^+/Li on asymmetric Li | SS coin cells. Cyclic voltammetry (CV) tests were performed at the same scan rate, with 5 scans ranging from −0.100 to 1.00 V versus Li^+/Li.

Chronopotentiometry tests were performed at the constant temperature of 30 °C on lithium symmetric coin cells, by applying seven values of current density spanning from 50 to 500 μA cm^{-2} for 10 h each, followed by a final control test at 100 μA cm^{-2}, to verify the integrity of QSE under stripping and plating (SP) condition, for a total of 70 SP complete cycles. Then, a constant current j_{curr} = 100 μA cm^{-2} was maintained until the failure of the device, to verify the long-term stability behavior of the QSEs.

Full cell tests were performed on coin cell constituted by lithium as anode and $LiFePO_4$ as cathodic material. Aluminium foil coated via doctor blading by a slurry made of lithium ferrous phosphate (LFP) (80 wt.%), SuperP carbon black (10 wt.%) and PVDF (10 wt.%) was prepared and vacuum heated at 100 °C before assembling the cell, with an average loading of active mass of 1.3 mg cm^{-2}. Galvanostatic Cycling with Potential Limitations (GCPL) analysis was performed at 30 °C at 0.1 C in the potential range 2.8 – 3.9 V versus Li^+/Li.

Supporting Information

Supporting Information is available from the Wiley Online Library or from the author.

Acknowledgements

This study was carried out within the MOST – Sustainable Mobility Center and received funding from the European Union Next-GenerationEU (PIANO NAZIONALE DI RIPRESA E RESILIENZA (PNRR) – MISSIONE 4 COMPONENTE 2, INVESTIMENTO 1.4 – D.D. 1033 17/06/2022, CN00000023). This manuscript reflects only the authors' views and opinions, neither the European Union nor the European Commission can be considered responsible for them. Part of the measurements were performed at R2BATT joint laboratory (at University of Pavia) funded by the Regione Lombardia (Project ECOCIRC).

Conflict of Interest

The authors declare no conflict of interest.

Data Availability Statement

The data that support the findings of this study are available from the corresponding author upon reasonable request.

Keywords

DFT, hybrid filler, $LiFePO_4$, lithium metal batteries, solid-state electrolyte, spectroscopy

Received: February 2, 2024
Published online:

[1] S. Xia, X. Wu, Z. Zhang, Y. Cui, W. Liu, *Chem* **2019**, *5*, 753.
[2] W. Xu, J. Wang, F. Ding, X. Chen, E. Nasybulin, Y. Zhang, J. G. Zhang, *Energy Environ. Sci.* **2014**, *7*, 513.
[3] D. Lin, Y. Liu, Y. Cui, *Nat. Nanotechnol.* **2017**, *12*, 194.
[4] K. Deng, D. Han, S. Ren, S. Wang, M. Xiao, Y. Meng, *J. Mater. Chem. A Mater.* **2019**, *7*, 13113.
[5] J. Qian, W. A. Henderson, W. Xu, P. Bhattacharya, M. Engelhard, O. Borodin, J. G. Zhang, *Nat. Commun.* **2015**, *6*.
[6] X. B. Cheng, R. Zhang, C. Z. Zhao, Q. Zhang, *Chem. Rev.* **2017**, *117*, 10403.
[7] R. C. Agrawal, G. P. Pandey, *J. Phys. D Appl. Phys.* **2008**, *41*.
[8] Y. Zhang, T. T. Zuo, J. Popovic, K. Lim, Y. X. Yin, J. Maier, Y. G. Guo, *Mater. Today* **2020**, *33*, 56.
[9] L. Long, S. Wang, M. Xiao, Y. Meng, *J. Mater. Chem. A Mater.* **2016**, *4*, 10038.
[10] B. Zhou, Y. H. Jo, R. Wang, D. He, X. Zhou, X. Xie, Z. Xue, *J. Mater. Chem. A Mater.* **2019**, *7*, 10354.
[11] P. Jaumaux, J. Wu, D. Shanmukaraj, Y. Wang, D. Zhou, B. Sun, F. Kang, B. Li, M. Armand, G. Wang, *Adv. Funct. Mater.* **2021**, *31*.
[12] Z. Xue, D. He, X. Xie, *J Mater Chem A Mater* **2015**, *3*, 19218.
[13] C. Li, Z. yu Wang, Z. jiang He, Y. jiao Li, J. Mao, K. hua Dai, C. Yan, J. chao Zheng, *Sustainable Materials and Technologies* **2021**, *29*.
[14] R. C. Agrawal, G. P. Pandey, *J Phys D Appl Phys* **2008**, *41*.
[15] G. P. Pandey, S. A. Hashmi, R. C. Agrawal, *Solid State Ion* **2008**, *179*, 543.
[16] Y. Kumar, S. A. Hashmi, G. P. Pandey, *Solid State Ion* **2011**, *201*, 73.
[17] Y. Wu, Y. Li, Y. Wang, Q. Liu, Q. Chen, M. Chen, *J. Energy Chem.* **2022**, *64*, 62.
[18] A. Magistris, E. Quartarone, P. Mustarelli, Y. Saito, H. Kataoka, *Solid State Ion* **2002**, *152*, 347.
[19] C. Capiglia, Y. Saito, H. Kataoka, T. Kodama, E. Quartarone, P. Mustarelli, *Solid State Ion* **2000**, *131*, 291.
[20] L. Mezzomo, R. Lorenzi, M. Mauri, R. Simonutti, M. D'Arienzo, T.-U. Wi, S. Ko, H.-W. Lee, L. Poggini, A. Caneschi, P. Mustarelli, R. Ruffo, *Nano Lett.* **2022**, *22*, 8509.

[21] X. Zhang, J. Han, X. Niu, C. Xin, C. Xue, S. Wang, Y. Shen, L. Zhang, L. Li, C. W. Nan, *Batter Supercaps* **2020**, *3*, 876.
[22] X. Zhang, S. Wang, C. Xue, C. Xin, Y. Lin, Y. Shen, L. Li, C. W. Nan, *Adv. Mater.* **2019**, *31*.
[23] D. Callegari, S. Bonizzoni, V. Berbenni, E. Quartarone, P. Mustarelli, *Adv. Mater.* **2020**, *32*.
[24] X. Zhang, S. Wang, C. Xue, C. Xin, Y. Lin, Y. Shen, L. Li, C. W. Nan, *Adv. Mater.* **2020**, *32*.
[25] N. Vallana, E. Carena, N. Ceribelli, L. Mezzomo, G. Di Liberto, M. Mauri, C. Ferrara, R. Lorenzi, G. Livia, R. Ruffo, P. Mustarelli, *ACS Applied Energy Materials*, https://doi.org/10.1021/acsaem/3c03046.
[26] B. A. Morrow, R. A. McFarlane, *J. Phys. Chem.* **1986**, *90*, 3192.
[27] B. A. Morrow, R. A. McFarlan, *Journal of Physical Chemistry* **1992**, *96*, 1395.
[28] L. Mezzomo, S. Bonato, S. Mostoni, B. di Credico, R. Scotti, M. D'Arienzo, P. Mustarelli, R. Ruffo, *Electrochim. Acta* **2022**, 411.
[29] S. Mostoni, M. D'Arienzo, B. di Credico, L. Armelao, M. Rancan, S. Dirè, E. Callone, R. Donetti, A. Susanna, R. Scotti, *Ind. Eng. Chem. Res.* **2021**, *60*, 10180.
[30] S. R. Culler, H. Ishida, J. L. Koenig, *J. Colloid Interface Sci.* **1985**, *106*, 334.
[31] C.-H. Chiang, H. Ishida, J. L. Koenig, *J. Colloid Interface Sci.* **1980**, *74*, 396.
[32] F. Moeinpour, A. Alimoradi, M. Kazemi, *J Environ Health Sci Eng* **2014**, *12*, 112.
[33] X. Jiang, X. Tang, L. Tang, B. Zhang, H. Mao, *Ceram. Int.* **2019**, *45*, 7673.
[34] S. Song, C. Peng, *J. Dispers. Sci. Technol.* **2005**, *26*, 197.
[35] A. S. Cattaneo, C. Ferrara, D. C. Villa, S. Angioni, C. Milanese, D. Capsoni, S. Grandi, P. Mustarelli, V. Allodi, G. Mariotto, S. Brutti, E. Quartarone, *Microporous Mesoporous Mater.* **2016**, *219*, 219.
[36] L. Barbieri, C. Leonelli, T. Manfredini, C. Siligardi, A. Bonamartini Corradi, P. Mustarelli, C. Tomasi, *J. Am. Ceram. Soc.* **1997**, *80*, 3077.
[37] R. Mueller, H. K. Kammler, K. Wegner, S. E. Pratsinis, *Langmuir* **2003**, *19*, 160.
[38] R. Scotti, L. Wahba, M. Crippa, M. D'Arienzo, R. Donetti, N. Santo, F. Morazzoni, *Soft Matter* **2012**, *8*, 2131.
[39] D. Selli, M. Tawfilas, M. Mauri, R. Simonutti, C. Di Valentin, *Chem. Mater.* **2019**, *31*, 7531.
[40] M. Maurel, T. Montheil, J. Martin, L. Chaar, V. Guzman-Gonzalez, M. Couvet, T. Jacquet, T. Jia, B. Eymin, K. Parra, P. Dumy, J. Martinez, F. Ruggiero, E. Vaganay, A. Mehdi, J. L. Coll, G. Subra, *Nanomaterials* **2021**, *11*, 177.
[41] K. Rahme, L. Chen, R. G. Hobbs, M. A. Morris, C. O'Driscoll, J. D. Holmes, *RSC Adv.* **2013**, *3*, 6085.
[42] T. C. Jao, I. Scott, D. Steele, *J. Mol. Spectrosc.* **1982**, *92*, 1.
[43] V. H. Paschoal, L. F. O. Faria, M. C. C. Ribeiro, *Chem. Rev.* **2017**, *117*, 7053.
[44] M. Maier, D. Abbas, M. Komma, M. S. Mu'min, S. Thiele, T. Böhm, *J. Memb. Sci.* **2023**, *669*, 121244.
[45] K. Fujii, H. Wakamatsu, Y. Todorov, N. Yoshimoto, M. Morita, *J. Phys. Chem. C* **2016**, *120*, 17196.
[46] Y. Umebayashi, K. Matsumoto, I. Mekata, S. Ishiguro, *Phys. Chem. Chem. Phys.* **2002**, *4*, 5599.
[47] J.-C. Lassègues, J. Grondin, D. Talaga, *Phys. Chem. Chem. Phys.* **2006**, *8*, 5629.
[48] P. Stigliano, C. Ferrara, N. Pianta, A. Gentile, L. Mezzomo, R. Lorenzi, V. Berbenni, R. Ruffo, G. B. Appetecchi, P. Mustarelli, *Electrochim. Acta* **2022**, *412*, 140123.
[49] Y. Yamada, M. Yaegashi, T. Abe, A. Yamada, *Chem. Commun.* **2013**, *49*, 11194.
[50] Y. Saito, H. Kataoka, E. Quartarone, P. Mustarelli, *J. Phys. Chem. B* **2002**, *106*, 7200.
[51] S. Zhou, S. Zhong, Y. Dong, Z. Liu, L. Dong, B. Yuan, H. Xie, Y. Liu, L. Qiao, J. Han, W. He, *Adv. Funct. Mater.* **2023**, *33*.
[52] C. Capiglia, P. Mustarelli, E. Quartarone, C. Tomasi, A. Magistris, *Solid State Ion* **1999**, *118*, 73.
[53] W. Liu, N. Liu, J. Sun, P.-C. Hsu, Y. Li, H.-W. Lee, Y. Cui, *Nano Lett.* **2015**, *15*, 2740.
[54] M. R. Johan, L. B. Fen, *Ionics (Kiel)* **2010**, *16*, 335.
[55] X. Tang, R. Muchakayala, S. Song, Z. Zhang, A. R. Polu, *Journal of Industrial and Engineering Chemistry* **2016**, *37*, 67.
[56] X. Liu, J. Liu, B. Lin, F. Chu, Y. Ren, *ACS Appl. Energy Mater.* **2022**, *5*, 1031.
[57] A. B. Puthirath, S. Patra, S. Pal, A. Puthirath Balan, N. Tharangattu N, *J. Mater. Chem. A Mater.* **2017**, *5*, 11152.
[58] S. Ramesh, T. Winie, A. K. Arof, *Eur. Polym. J.* **2007**, *43*, 1963.
[59] H. Matsui, T. Nakamura, Y. Kobayashi, M. Tabuchi, Y. Yamada, *J. Power Sources* **2010**, *195*, 6879.
[60] D. Ouyang, M. Chen, J. Weng, K. Wang, J. Wang, Z. Wang, *J. Energy Chem.* **2023**, *81*, 543.
[61] W. Stober, A. Fink, E. Bohn, *J. Colloid Interface Sci.* **1968**, *26*, 62.
[62] L. Tripaldi, E. Callone, M. D'Arienzo, S. Dirè, L. Giannini, S. Mascotto, A. Meyer, R. Scotti, L. Tadiello, B. di Credico, *Soft Matter* **2021**, *17*, 9434.
[63] G. Kresse, J. Furthmüller, *Phys. Rev. B* **1996**, *54*, 11169.
[64] J. P. Perdew, K. Burke, M. Ernzerhof, *Phys. Rev. Lett.* **1996**, *77*, 3865.
[65] P. E. Blöchl, *Phys. Rev. B* **1994**, *50*, 17953.
[66] G. Di Liberto, L. Giordano, *Electrochemical Science Advances* **2023**.
[67] L.-M. Liu, C. Zhang, G. Thornton, A. Michaelides, *Phys. Rev. B* **2010**, *82*, 161415.
[68] W. G. Hoover, *Phys Rev A (Coll Park)* **1985**, *31*, 1695.
[69] S. Nosé, *J. Chem. Phys.* **1984**, *81*, 511.
[70] G. Di Liberto, G. Pacchioni, Y. Shao-Horn, L. Giordano, *J. Phys. Chem. C* **2023**, *127*, 10127.
[71] M. J. Frisch, G. W. Trucks, H. B. Schlegel, G. E. Scuseria, M. A. Robb, J. R. Cheeseman, G. Scalmani, V. Barone, G. A. Petersson, H. Nakatsuji, X. Li, M. Caricato, A. V. Marenich, J. Bloino, B. G. Janesko, R. Gomperts, B. Mennucci, H. P. Hratchian, J. V. Ortiz, A. F. Izmaylov, J. L. Sonnenberg, D. Williams-Young, F. Ding, F. Lipparini, F. Egidi, J. Goins, B. Peng, A. Petrone, T. Henderson, D. Ranasinghe, et. al., Gaussian, Inc., Wallingford CT, **2016**.
[72] J. Tomasi, B. Mennucci, R. Cammi, *Chem. Rev.* **2005**, *105*, 2999.
[73] M. Cossi, N. Rega, G. Scalmani, V. Barone, *J. Comput. Chem.* **2003**, *24*, 669.
[74] F. He, W. Tang, X. Zhang, L. Deng, J. Luo, *Adv. Mater.* **2021**, *33*.